Received: 16 November 2023 | Revised: 19 March 2024 | Accepted: 10 April 2024

IET Electric Power Applications

DOI: 10.1049/elp2.12439

The Institution of Engineering and Technology WILEY

ORIGINAL RESEARCH

Ultra-fast finite element analysis of coreless axial flux permanent magnet synchronous machines

Yaser Chulaee | **Dan M. Ionel**

SPARK Laboratory, Stanley and Karen Pigman College of Engineering, University of Kentucky, Lexington, Kentucky, USA

Correspondence

Yaser Chulaee.
Email: yaser.chulaee@uky.edu

Funding information

National Science Foundation, Grant/Award Number: #1809876; University of Kentucky

Abstract

Large-scale design optimisation techniques enable the design of high-performance electric machines. Electromagnetic 3D finite element analysis (FEA) is typically employed in optimisation studies for accurate analysis of axial flux permanent magnet (AFPM) machines, which require extensive computational resources. To reduce the computational burden, a FEA-based mathematical method relying on the geometric and magnetic symmetry of coreless AFPM machines is proposed to estimate the machine performance indicators using the least number of FEA solutions, thereby significantly lowering the running time. This method is generally applicable to AFPM machines with low saturation effects and cogging torque as exemplified for a printed circuit board (PCB) stator coreless AFPM machine. To further reduce the computation time, a systematically simplified equivalent 3D FEA model for planar PCB coils integrated with this machine is also proposed. The practical implementation of the introduced method is elaborated based on an example optimisation study, and an analytical method for fast design scaling is also discussed. The results of the proposed approach are compared with detailed transient FEA results, and a prototype 26-pole PCB stator coreless AFPM machine was also used to validate the results experimentally.

KEYWORDS

AC machines, electric motors, electromagnetic fields, finite element analysis, modal analysis, optimisation, permanent magnet machines, permanent magnet motors

1 | INTRODUCTION

For designing high-performance electric machines, large-scale design optimisation approaches with multiple independent dimensional variables and conflicting objectives are widely used. A large-scale model-based design optimisation process consists of a machine model for evaluating performance indicators and an optimisation algorithm for seeking the optimal global designs. Finite element analysis (FEA) has been established as the method of choice for detailed studies of the electric machine with complex geometries and materials and has been extensively employed for optimisation in recent years [1–6]. The parameterised finite element (FE) model is adjusted to increase specific performance metrics regarding the application requirements. Power loss, cost, torque and power densities, torque ripple, and power factor are typical performance measures that comprise an optimisation problem's objectives and constraints.

Finite element analysis models require extensive computing power and typically have long running times, which limits their effectiveness in large-scale design optimisation problems. Population-based evolutionary algorithms are usually applied for the optimal design of electric machines, with the differential evolution (DE) approach being a popular option. Conventional DE has the drawback of requiring the evaluation of a large number of generations and candidate designs; for example, a design optimisation problem for a brushless PM synchronous machine with five independent variables demanded the analysis of almost four thousand candidate designs [7].

In recent years, new techniques have been introduced to reduce the running time of FE machine models and speed up optimisation algorithms, as described in the works of Rosu

et al. [1], Taran et al. [7], and Sato and Igarashi [8]. The most common solution to the aforementioned issue is to employ 2D FE models of electric machines with lower complexity [9]. Analytical methods for the analysis of the airgap magnetic field can also be considered as described, for example, by Xia et al. in ref. [10].

The analysis of skew angle, overhang, or end coils in machines with 3D flux pathways, such as axial flux PM machines (AFPM), has revealed that 2D models and analytical methods are not sufficiently accurate [7, 11–14]. A detailed modelling of the machine is required in any case to study the eddy current losses in the stator winding. Therefore, there is a need for ultrafast 3D FE models for AFPMSMs that can support performance analysis, large-scale parametric studies, and design optimisations.

The history of ultrafast or simplified FE models goes back decades; a brief review has been provided by Ionel and Popescu in ref. [15] and further developed in ref. [16]. More recent developments over the last decade will be briefly mentioned in the following. A novel computationally efficient modelling method for hybrid excitation synchronous machines with radial/axial flux paths via magnetic equivalent circuit (MEC) was proposed by Liu et al. in ref. [17].

A fast method to calculate iron loss and magnet loss caused by pulse width modulation (PWM) in a voltage source inverter (VSI) fed axial flux PM machine with 3D geometry, using a state space model and multislice 2D model presented by Sergeant et al. in ref. [18]. A field reconstruction method for induction machine simulation that utilises a small number of finite-element evaluations to establish basis functions of normal and tangential flux densities was introduced by Wu et al. in ref. [19]. A d-q-based simplified approach was introduced by Bianchi and Alberti in ref. [20]. Other fast FE models developed for PMSM analysis and design considering iron loss, temperature variations, saturation effects are introduced by Chen et al. [21], Lin et al. [22], Billah et al. [23], and Candelo-Zuluaga et al. [24].

A design optimisation method employing an ultrafast, computationally efficient FE analysis technique was developed by Sizov et al. in ref. [25]. In their technique, a minimum number of magnetostatic solutions is used for the analysis, which makes it possible to study thousands of candidate motor designs. Other examples of the computationally efficient FE models incorporated in design optimisation studies are presented by Zarko et al. [26] and Wang et al. [27].

Among the various types of AFPMSMs, the coreless stator type offers unique features as it eliminates magnetic cores and their related losses, leading to zero cogging torque and a uniform torque profile, reduced weight, and lower audible noise and vibration [28–30]. These factors collectively contribute to increased overall efficiency and specific torque (Nm/kg).

The integration of printed circuit board (PCB) stators in coreless AFPM machines has become a popular topic of discussion. PCB stators allow for modularity and phase separation for increased fault tolerance. Coil shapes can be designed with a great deal of freedom, and the fabrication process is, in principle, reliable and repeatable [31–33]. Integrating PCB stators in coreless AFPM machines adds more complexity to the machine model, and planar PCB traces should be meticulously modelled in order to accurately predict the performance of such machines. Narrow traces need fine meshing, which results in a high number of tetrahedral elements and consequently a high computational burden [34]. Therefore, automating the large-scale design optimisation of such machines would be challenging, emphasising the need for a simplified, computationally efficient model of a coreless AFPM machine with a PCB stator.

According to Marcolini et al., due to the complexity of PCB winding geometry and loss mechanisms, the design procedure cannot be easily automated with an optimisation algorithm [35]. This led the authors to develop machine geometries using an ad-hoc technique composed of a few easy stages. The magnetic and geometric parameters of a PCB stator AFPM machine are analytically derived and optimised using a genetic algorithm by Tokgoz et al. in refs. [36, 37]. In this study, the FE analysis was only performed to verify the selected design.

Analytical calculation methods are employed by Wang et al. to optimise the geometric dimensions of a coreless AFPM machine's hexagonal concentric PCB stator coil to obtain the maximum ratio of torque to copper loss and the 3D FEA method was only used as a reference for preliminary design [38]. No papers on the specific topic of automated design optimisation of coreless AFPM machines with planar PCB conductors employing accurate, detailed 3D FE models and population-based evolutionary algorithms were identified by the literature search, and this current paper fills in the research gap by introducing a systematic, computationally efficient FEA-based approach.

This paper initially proposes a systematic approach to determining the minimum required number of transient FEA solutions to predict the machine performance indices. Then, a simplified equivalent 3D FE model of a planar PCB coil integrated with a coreless AFPM machine is introduced. The combination of the two drastically reduces the computation time while maintaining an acceptable level of precision for performance assessment, allowing for the design optimisation of coreless PCB stator AFPM machines based on the evaluation of 3D FE models for hundreds of candidate designs. An example optimisation study is used to illustrate how the introduced method might be put into practice. It is important to highlight that the proposed approach is generally suitable for AFPM machines characterised by low saturation effects and cogging torque, as exemplified in this paper for a PCB stator coreless AFPM machine.

Section 2 describes the systematic approach for the estimation of machine performance with the minimum number of FEA solutions. In Section 3, the concept of a simplified equivalent 3D FE model of a planar PCB coil stator is explained. Experimental results to validate the proposed method are reported in Section 4. The example optimisation study employing the proposed approach, alternative torque calculation methods, an analytical approach for fast design scaling, and some technical implementation aspects are discussed in Section 5.

2 | ELECTROMAGNETIC FIELD, BACK-EMF, AND TORQUE ANALYSIS

In this section, a FEA-based mathematical approach is developed to find the least required number of FEA solutions for the performance evaluation of AFPM machines with coreless stators. In this research, a three-phase, double-rotor, single PCB stator, coreless AFPM machine is considered a case study for analysis and optimisation. The machine configuration with a spiral-shaped coil shown in Figure 1 is one of the most common structures of AFPM. This structure is often selected for its low torque ripple and high specific power [30, 39]. The specifications of the machine under study are tabulated in Table 1.

Lack of a magnetic core and, consequently, saturation effects result in reduced harmonic content in the machine waveforms. This allows for predicting the machine's performance with fewer FE analysis solutions. This paper presents a systematic approach to achieve the most accurate and computationally efficient results. The proposed method is generally applicable even in the presence of marginal saturation due to some special designs as discussed in Section 5.

The absence of saturation in a coreless AFPM machine was investigated by studying the machine under various conditions through FEA-based parametric studies, as illustrated in Figure 2. The initial study reveals that over a wide range of input currents, the output torque exhibits linear changes, even up to multiple times of the rated torque, highlighting the absence of saturation effects. Furthermore, it was observed that beyond a certain minimum thickness of rotor back iron, variations in back iron thickness do not affect the machine's torque production capability [40].

Due to the symmetry of the machine geometry and the periodicity of the magnetic flux as shown in Figure 3, only one pole, that is, 1/26 of the machine, is needed to evaluate the machine performance. Moreover, because of the symmetry of flux lines in the axial direction as illustrated in Figure 4, only one half of the model needs to be simulated in this direction. In Ansys Maxwell, these can be achieved by considering proper symmetry boundaries [41]. The simplifications described prior cut the computing load in half while maintaining result accuracy.

It should be noted that in the aforementioned configuration (Figure 4), three independent PCB stators are stacked together in the axial direction, each dedicated to one phase. They are mechanically shifted with respect to each other by the equivalent of 120 electrical degrees to form a three-phase machine. This configuration facilitates observing the machine periodicity. Alternatively, all phases can be implemented on a single plane either as a PCB or conventional Litz wire as demonstrated in Figure 5, for a 24-coil, 18-pole coreless AFPM machine.

In selecting the minimum portion of the machine that needs to be modelled, one has to ensure the minimum periodicity is observed. In the case of the machine shown in Figure 5, three coils (one per phase) and two poles need to be considered. Detailed explanations to further reduced the computation time in such configurations have been presented in refs. [15, 16]. It is worth mentioning that in a coreless machine, regardless of the number of coils and poles, the lack of

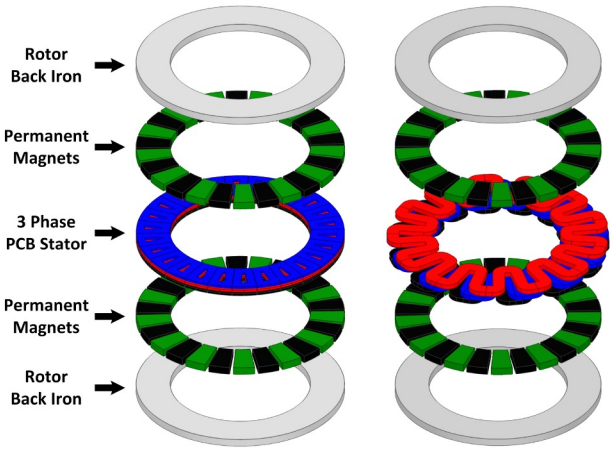

FIGURE 1 Exploded views of the 3D finite element analysis models of the example 26-pole, three-phase, double-rotor, single-stator coreless AFPM machine with spiral and wave printed circuit board stator windings are shown. The machine on the left side, with the more common spiral-shaped PCB coils is studied in this paper.

TABLE 1 Specifications and main dimensions for the studied three-phase double-rotor single-stator coreless PCB stator AFPM machine.

Parameter	Value	Unit
Rated power	4.2	kW
Rated speed	2100	rpm
Airgap (magnet to PCB)	1.0	mm
Rotor outer diameter	304	mm
Rotor inner diameter	208	mm
Stator outer diameter	310	mm
Stator inner diameter	202	mm
No. of rotor poles	26	-
No. of stator coils	26	-

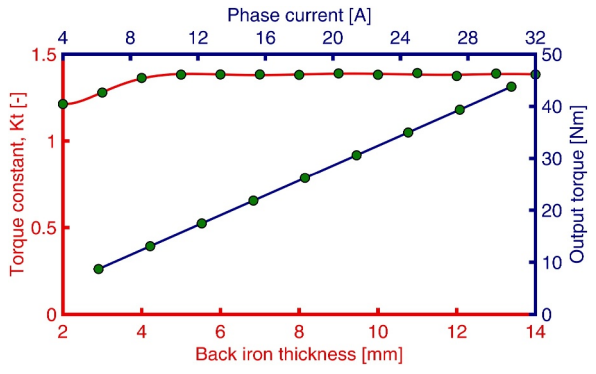

FIGURE 2 Results of parametric studies on the machine under investigation, illustrating the absence of saturation effects in coreless AFPM machines.

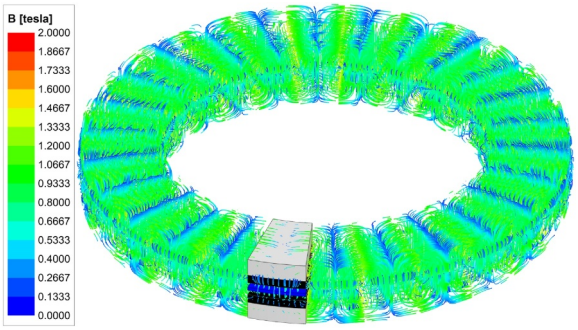

FIGURE 3 Full model flux density lines of the studied 26-pole, three-phase, double-rotor, single-stator, coreless AFPM machine out of 1/26 of the machine model using symmetry boundaries.

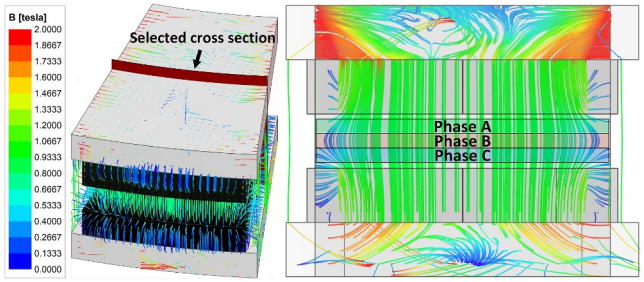

FIGURE 4 Flux density lines across a cross section of this machine show the symmetry of flux path in the *z* direction and also the fringing effect within the airgap.

saturation effects and therefore the low harmonics in the machine waveforms are expected. Hence, the proposed method is generally applicable as described in the section below.

In the following, different performance indices of the machine under study are calculated through the proposed method. A fair foundation for comparison was ensured by employing identical geometry, mesh elements, and material models for the time-stepping FEA of the machine model with the real coil shape. It is worth mentioning that in the following, 'one electrical cycle' corresponds to one electrical cycle of the supplied sinusoidal current waveform to a given single phase. Additionally, since this machine operates with 13 pole pairs, one electrical cycle corresponds to 1/13 mechanical cycles.

2.1 | Flux linkage and Back-EMF

The stator flux linkage waveform of the machine resulting from a transient FE analysis with 36 time steps is shown in Figure 6. The general expression of this flux linkage waveform generated by one phase can be written as follows:

$$\lambda(\theta) = \lambda_0 + \sum_{k=1}^{M} \lambda_k \cos(k\theta + \phi_k), \tag{1}$$

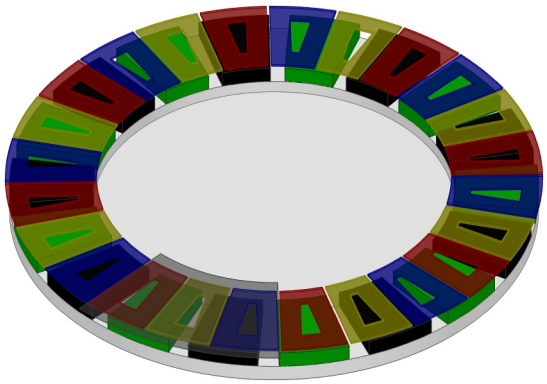

FIGURE 5 A three-phase 24-coil 18-pole coreless AFPM machine that all coils are placed on one plane. The minimum periodicity of the machine model is highlighted.

where

$$\lambda_0 = \frac{1}{\pi}\int_0^{\pi} \lambda(\theta)\ \mathrm{d}\theta,$$
$$\lambda_k = \frac{2}{\pi}\int_0^{\pi} \lambda(\theta)\ \cos k\theta\ \mathrm{d}\theta, \tag{2}$$

θ is rotor position in electrical degrees, and ϕ is the initial degree for each phase.

The harmonic content of the waveform shown in Figure 6, derived from a conventional Fourier series analysis is tabulated in Table 2. Because of the even symmetry of this waveform, all sinusoidal components (b_k coefficients) are zero.

According to the Nyquist theorem, to derive all Fourier components of a periodic waveform, the sampling frequency must be at least twice the highest waveform frequency component:

$$f_s \geq 2f_m, \tag{3}$$

where f_m denotes the maximum harmonic frequency. Therefore, to construct a waveform, the number of samples, that is, FE solutions, must be equal to or greater than twice the maximum order of harmonics in that waveform:

$$s \geq 2M, \tag{4}$$

where s is the number of FEA solutions and M is the maximum harmonic order in the waveform.

Thereby, to accurately derive the flux linkage waveform with $M = 1$, at least two FEA solutions are required. This approach, which avoids unnecessary FEA solutions drastically reduces the model analysis time while maintaining the accuracy of the results. So, the general expression is simplified as follows:

$$\lambda(\theta) = \lambda_0 + \lambda_1 \cos(\theta + \phi_1). \tag{5}$$

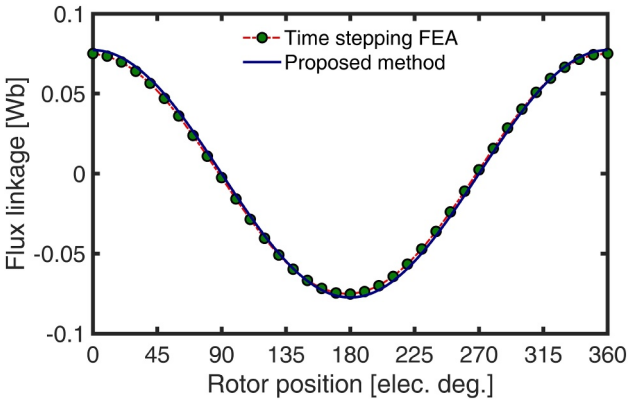

FIGURE 6 Flux linkage waveforms result from transient FEA and the proposed method, that is, Equation (5) with only two FEA solutions. The back-EMF can be calculated by taking a derivative of the flux linkage. FEA, finite element analysis.

TABLE 2 Harmonic content of the single-phase torque and flux linkage waveforms over an electrical cycle derived from Fourier series analysis. All harmonic orders higher than four are virtually zero.

Harmonic order	a_0	a_k	b_k	Unit
DC component	0.00	-	-	Wb
	6.23	-	-	N.m
First	-	0.08	0.00	Wb
	-	0.00	0.00	N.m
Second	-	0.00	0.00	Wb
	-	−6.32	0.00	N.m
Third	-	0.00	0.00	Wb
	-	0.00	0.00	N.m
Fourth	-	0.00	0.00	Wb
	-	0.11	0.00	N.m

The calculated flux linkage waveform within one electrical cycle with only two FEA solutions at 0 and 90 electrical degrees is shown in Figure 2. This figure illustrates that there is a very good agreement between the calculated waveform based on the proposed method and time stepping FE analysis.

The back-EMF can be calculated from the derivative of the flux linkage waveform as generally expressed in the following:

$$E(\theta) = -\frac{\mathrm{d}\lambda}{\mathrm{d}\theta}\frac{\mathrm{d}\theta}{\mathrm{d}t}\frac{n_1}{n_2} = \omega\sum_{k=1}^{M} k\frac{n_1}{n_2}\lambda_k \sin(k\theta+\phi). \quad (6)$$

It should be noted that the back-EMF of the equivalent coil introduced in the following section should be scaled by the number of turns ratio, that is, n_1/n_2, where n_1 and n_2 are the number of turns of the real and equivalent coils, respectively. The calculated single coil back-EMF by Equation (6) with only two FE solutions is demonstrated in Figure 7.

2.2 | Electromagnetic torque

Following the same procedure presented in the previous section, the torque waveform can also be derived using the minimum number of FEA solutions. The harmonic analysis of the torque waveform, with a period of 360 electrical degrees, reveals that the DC component and the second harmonic constitute the majority of the harmonic content, with the fourth harmonic accounting for only 1.7% of the second harmonic and all other orders being negligible.

Therefore, to further reduce computational time, harmonic orders higher than two, which comprise only 1.7% of the dominant component, can be neglected, resulting in $M = 2$. Since the torque waveform repeats every 180 electrical degrees, we intuitively know that only two FEA solutions are required, similar to the flux linkage waveform. So the general expression for torque waveform is written as follows:

$$T_{em}(\theta) = T_{em,0} + T_{em,1}\cos(\theta+\phi_1), \quad (7)$$

The estimated waveform with this method is highly comparable with time-stepping FEA results as depicted in Figure 8.

2.3 | Multi phase operation

One approach for multiphase operation is to have one PCB per phase, as is the case with the machine under study. To form the total output torque profile, PCB stators are rotated by 90 and 120 electrical degrees with respect to each other in two-phase and three-phase configuration, respectively. The total output torque is derived from adding single phase torque waveforms and for the three-phase configuration it can be written as follows:

$$T_{em} = T_{em,A} + T_{em,B} + T_{em,C}, \quad (8)$$

where

$$\begin{aligned} T_{em,A}(\theta) &= T_{0,A} + \sum_{k=1}^{k=M} T_{k,A}\cos[k\theta+\phi_k], \\ T_{em,B}(\theta) &= T_{0,B} + \sum_{k=1}^{k=M} T_{k,B}\cos[k(\theta+120)+\phi_k], \\ T_{em,C}(\theta) &= T_{0,C} + \sum_{k=1}^{k=M} T_{k,C}\cos[k(\theta+240)+\phi_k]. \end{aligned} \quad (9)$$

In this configuration, which is the most unfavourable situation in terms of torque ripple, PCB stators are axially stacked within the magnetic airgap (rotor to rotor distance) as demonstrated in Figure 4. Due to the wide magnetic airgap in such machines, stator conductors are exposed to uneven magnetic flux distribution resulting from the fringing effect. Hence, the single-phase output torque is not exactly the same, and it leads to a torque ripple that is based on Equations (8) and (9) which can be calculated as follows:

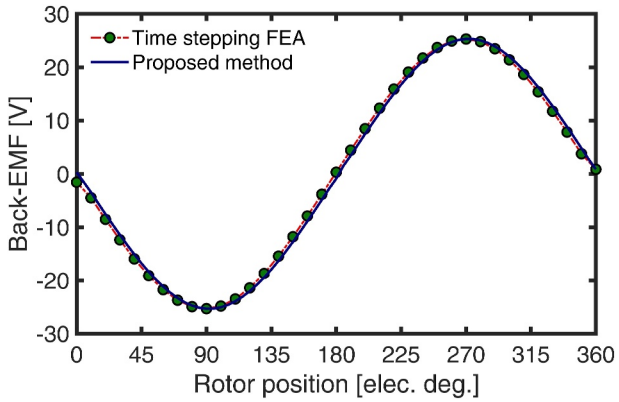

FIGURE 7 Single coil back-EMF of the real coil model and the estimated back-EMF of the simplified coil scaled by the ratio of the number of turns based on Equation (6).

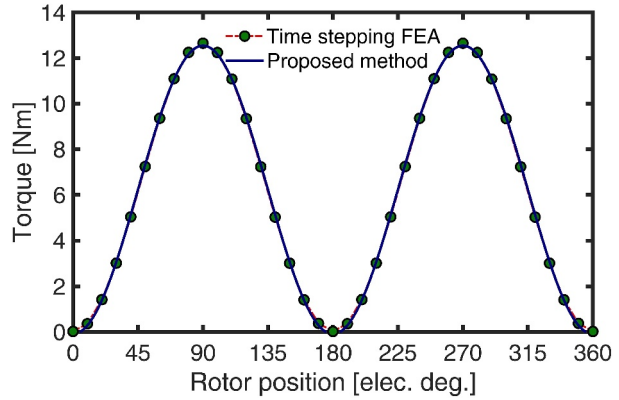

FIGURE 8 The single-phase output torque results from a transient finite element analysis with 36 time steps and an estimated waveform based on the Equation (7) within one electrical cycle.

$$T_{rp} = \frac{\sum_{k=1}^{k=M} \left(2T_{k,A} - T_{k,C} - T_{k,C}\right) \cos(k\theta + \phi_k)}{T_{0,A} + T_{0,B} + T_{0,C}}. \quad (10)$$

It should be noted that due to a lack of stator teeth, the cogging torque in coreless machines is virtually zero.

For an output three-phase torque of 19 Nm, the maximum output torque of phases A and C shown in Figure 4 is 2.2% higher than the middle phase, B, and it leads to a torque ripple of 1.4% for all three phases. The single phase and total output torque waveforms are illustrated in Figure 9.

In order to capture this insignificant amount of torque ripple, all three phases need to be modelled, and each phase requires a lot of meh elements. Thus, to further reduce the FEA computational burden, just one phase needs to be modelled to predict the output electromagnetic torque of the multi-phase machines. In this case, finer mesh can be considered for conductors within one phase to improve the accuracy of the results.

2.4 | Stator windings losses

Coreless machines potentially offer superior efficiency compared to conventional cored machines by eliminating the magnetic core and its associated power losses. Furthermore, power losses in the rotor magnets are negligible due to the very low armature reaction. As a result, the primary source of power loss lies in the stator windings. Minimising these losses must be a key consideration in the machine design process.

The main components of stator winding losses include Joule losses (i.e. RMS phase current ohmic losses), eddy current losses, and circulating current losses. As illustrated in an example provided in ref. [42] by the same group of authors as this paper, in an integral horsepower PCB stator coreless AFPM machine delivering 19 Nm at 2100 rpm, stator winding losses account for approximately 83% of total power losses, with Joule losses specifically comprising about 70%. This underscores the significance of minimising them in the design procedure.

Finite element analysis software, such as Ansys Maxwell, employed in this research, can calculate ohmic losses, along with various other loss components and performance indices, including eddy current losses, hysteresis losses, and output torque. In the case of Joule loss, the software calculates it by considering the determined winding material, typically copper, and the coil geometry. For a sinusoidal input current, solving the FE model for only two steps, that is, $\theta_e = 0$, and $\theta_e = 90$, zero and maximum input current is satisfactory to find the Joule losses.

It is important to note that to derive the total Joule losses, the FEA-based calculated losses may need to be scaled, taking into account the total number of coils and phases. Additionally, if a simplified coil model is used in this step, the calculated losses must be scaled based on the ratio of the slot fill factors (SFF) as discussed in the next section in detail. The phase resistance can also be calculated by dividing the Joule losses by the RMS value of the sinusoidal input current.

In the coreless machines, where there is no magnetic core in the stator, the copper conductors are directly exposed to fluctuations in the airgap's magnetic flux density. This exposure can lead to potentially high power losses in the stator conductors caused by eddy currents. Furthermore, machines with a wide magnetic airgap suffer from an uneven distribution of magnetic flux density and notable flux fringing. Consequently, parallel conductors experience varying induced voltages, resulting in circulating current losses. These loss mechanisms are discussed at length in the previous paper from the authors [43].

Investigating eddy current and circulating current losses necessitates comprehensive models that account for precise turn-by-turn stator coils and all interconnections. Developing such parametric 3D FEA models is exceedingly time-consuming and demands substantial computational resources. Consequently, integrating such analyses into large-scale design optimisations, which involve evaluating hundreds of models, is impractical, particularly on standard workstations.

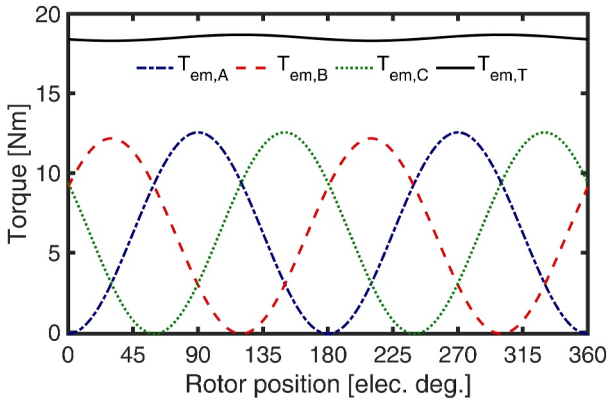

FIGURE 9 Total output torque is calculated by adding single-phase torque waveforms. The absence of stator teeth in coreless machines results in zero cogging torque. Airgap flux density variations result in different flux linkages in the phase windings, ultimately leading to a slight torque ripple.

Therefore, the alternative approach is to initially design and optimise the machine geometry, including rotor and stator dimensions, magnet shape, airgap, and coil envelope, utilising the proposed ultra-fast model with simplified coil geometry. This approach can accommodate a wide range of objectives, such as minimising Joule losses, cost, and weight, depending on the application requirements.

Subsequently, considering parameters such as airgap flux density, rated speed, the required back-EMF, and the optimised coil envelope, the number of turns and coils per phase and the number of parallel strands are determined. In this step, the ampere-turns per coil are kept constant, and the Joule losses of the designed coil can be calculated using the ratio of SFFs of actual and initially simplified coil as described in the next section. It should be noted that the optimisation algorithm guarantees the given coil envelope leads to minimal Joule losses (if selected as an objective), considering all other dimensions.

This multi-step approach was previously practically employed by the same group of authors, as demonstrated in ref. [42], to design a highly efficient 4.2 kW coreless axial flux PM machine. Following this design procedure, the authors achieved a machine with approximately 96% efficiency, with the rated eddy current loss comprising only about 13% of the total power losses, while circulating current losses were virtually eliminated through the use of a novel layer transposition technique.

Another typical source of power losses within the stator windings is the skin and proximity effects. The skin effect refers to the tendency of high-frequency currents to travel along the outer surface of a conductor, increasing resistance. The proximity effect involves the undesirable flow of current in alternate patterns, such as loops or concentrated distributions, caused by the magnetic fields produced by nearby conductors [44–46].

The absence of the skin effect in very narrow copper traces on the PCB stator or equivalent Litz wires was explained in refs. [32, 47]. This is because the skin depth at the rated frequency (less than 1 kHz) is considerably higher than the diameter of the conductors. Hence, there is no increase in copper losses across the speed range due to AC resistance within the studied machine.

The proximity effect in coreless AFPM machines is typically negligible due to a wide magnetic airgap and very low armature reaction. To further investigate its presence between coils in different layers, the flux linkage of the coil in the middle layer was monitored through FEA at two different states: first, with all other coils excited with the rated current, and second, with them not excited. As there was no difference in the monitored flux linkage, it can be stated that the proximity effect in the stator winding of coreless AFPM machines is negligible. This finding was also demonstrated for coreless AFPM machines by researchers in ref. [32].

3 | SIMPLIFIED 3D FE MODEL OF a PCB COIL

To determine the minimum required length of mesh elements for the machine model, generally a mesh convergence study is carried out. The result of an example study is shown in Table 3 with zero torque at zero electrical degrees and the symmetry of the waveform as convergence criteria. The tetrahedral mesh elements during the mesh convergence study at an example point are illustrated in Figure 10. It is worth mentioning that a copper trace represents a single wire in conventional stator windings, and a turn represents a closed loop of such conductor traces.

Following the same procedure, the real coil model needs more than 1.7 million tetrahedral elements as reported in Table 4. Due to the narrow dimensions of the PCB traces, there are an extremely high number of mesh elements, so the transient analysis with 36 steps (every 10 electrical degrees) takes more than three hours, or about six minutes per solution, on an Intel Xeon 3.5-GHz workstation.

It is challenging to evaluate a wide range of candidate designs with long running times in search of optimal coil geometry and rotor dimensions to meet the design requirements. Hence, finding a simplified, highly accurate FE model to assess machine performance indicators is one of the main subjects of this paper. 'Macro coil' modelling has been proposed in previous research papers to model stator coils as a solid block to cut down on machine model computation time [4, 34]. In this approach, coils are modelled like blocks with the dimensions of the coil envelope and because of the substantially lower complexity of the model, the running time is considerably lower than the real coil turn-by-turn model.

An example macro coil with input current density vectors is shown in Figure 11c. The analysis results relying on this block coil for the machine under study show that the number of tetrahedral elements and consequently the running time of this model are considerably lower than the detailed turn-by-turn model as reported in Table 4.

TABLE 3 The results of the mesh convergence study to find the minimum number of mesh elements for the simplified 6-turn equivalent coil model. The ratio of $T_\theta = 0$ to $T_\theta = 90$, which is denoted by error is one of the convergence criteria.

No. of tetrahedral elements	$T_{\theta\,=\,0}$ [Nm]	$T_{\theta\,=\,90}$ [Nm]	Error [%]
3,948,606	0.00	12.68	0.0
2,728,470	0.00	12.66	0.0
1,101,987	0.01	12.66	0.0
534,685	0.01	12.67	0.0
219,461	−0.27	12.51	2.1
133,204	−0.26	12.37	2.2
114,558	0.37	12.60	2.9

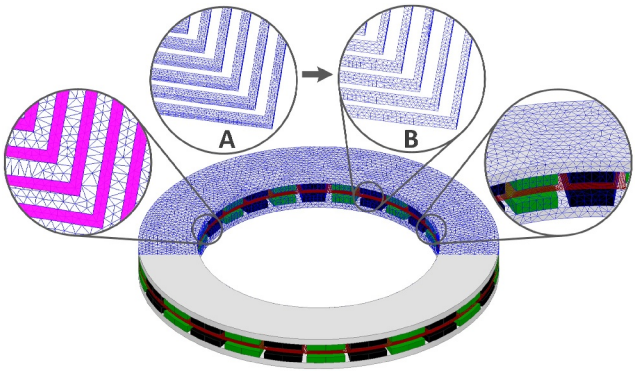

FIGURE 10 The tetrahedral mesh elements on the stator conductors, in between them, and magnets. The zoomed-in views marked as A and B show mesh elements on the traces at two points during the mesh convergence study.

TABLE 4 Comparing the accuracy of performance prediction and computational time for several simplified coil (reduced turn) models with the real coil model.

No. of turns	Tetrahedral elements	Running time per solution	Torque error [%]	Back-EMF error[%]	Joule loss error[%]
18	1,721,397	05:42	Ref.	Ref.	Ref.
10	712,486	02:18	1.51	1.35	1.47
8	606,433	02:01	2.06	2.09	2.29
6	534,685	01:54	2.74	2.99	3.11
4	450,275	01:36	6.96	6.96	5.78
Macro	424,844	01:12	4.08	3.17	9.42

The Macro coil model does not properly resemble the current density vector trajectories and gaps between traces as they are in the real coil model, especially at both end coils, where the current vectors are distorted in terms of both magnitude and direction. Therefore, it leads to a 4% error in the calculated maximum torque, and the estimated Joule losses have more than a 9% error when considering the results of the detailed 18-turn model as a reference. This error reduces as the number of turns in the simplified model increases and becomes closer to the real coil shape. So, this equivalent block model is not a viable candidate for estimating Joule losses and, to a lesser extent, torque and back-EMF due to over-simplification, at least for narrow PCB traces. This error reduces as the coil shape becomes more like the real coil.

To ensure accurate results, it is crucial that the simplified model's current density distribution closely resemble that of the real coil model. For that purpose, a systematic approach seeking a reduced-turn equivalent coil is proposed. The results of an example systematically exploring the proper simplified equivalent coil are tabulated in Table 4. In this study, the running time and three main performance indicators for 4-turn up to 10-turn and macro equivalent coils are investigated. Results show that there is a trade-off between the accuracy of the performance estimation and the running time.

Within these results, the 6-turn coil is intuitively the optimal equivalent coil because both the computational time and result accuracy are within an acceptable range. This model cuts the computational time by about 70% and keeps the estimation errors below 3%. This is due to the fact that the current density vectors of the reduced-turn coil follow the same pattern as the real coil model as demonstrated in Figures 11a and 11b, respectively. The combination of this simplified equivalent coil and the proposed method with the minimum number of FEA solutions substantially reduces the computational burden.

Throughout this research, single-layer PCB coils with the thickness of single-phase stator have been studied to mitigate complexity and shorten computation times. In practice, PCB stators benefit from multi-layer configurations that have narrow copper layers vertically connected through via holes with insulation layers between them. An example cross section of a real PCB coil side with 6 turns and 8 layers is demonstrated in Figure 12. A basis for scaling the FEA-driven Joule losses based on the simplified equivalent coil to that of the real coil is therefore needed. The coil envelope dimensions, meaning the inner and outer diameters as well as the coil width and thickness, are known to be the same in both cases. Some of these key dimensions are highlighted in Figure 11d.

The Joule losses within one PCB coil can be written as a function of the current density and SFF:

$$P_{cu} = J^2 \cdot A_t^2 \cdot \frac{\rho \cdot N_t \cdot N_L \cdot L_m}{A_t} = J^2 \cdot A_t \cdot \rho \cdot N_t \cdot N_L \cdot L_m$$

$$= J^2 \cdot \frac{A_c \cdot SFF}{N_t \cdot N_L} \cdot \rho \cdot N_t \cdot N_L \cdot L_m = J^2 \cdot A_c \cdot SFF \cdot \rho \cdot L_m, \tag{11}$$

where

$$J = \frac{I}{A_t} = \frac{N_t \cdot N_L \cdot I}{A_c \cdot SFF}, \tag{12}$$

and A_t and A_c are the trace and coil side cross section areas, respectively. The number of turns per layer, the number of

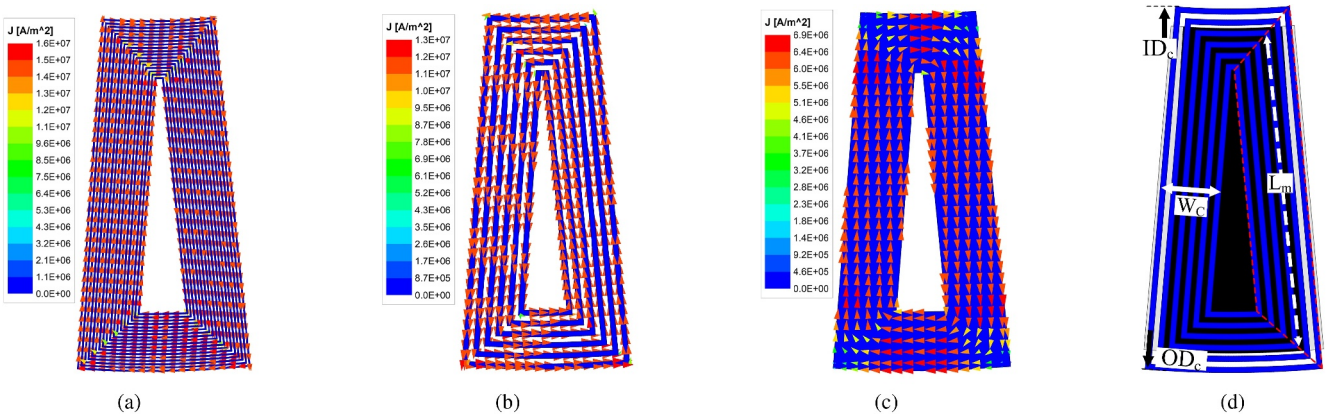

FIGURE 11 Input current density vectors in (a) real 18-turn coil, (b) 6-turn proposed equivalent coil, and (c) block coil. In contrast to the proposed simplified turn-by-turn coil model, the current density vectors at both ends of the coil in the block model are deformed, both in terms of magnitude and direction. The main dimensions of the coil envelope, that is, inner diameter (ID_c), outer diameter (OD_c), average radial length (L_m), and coil width (W_C) (d).

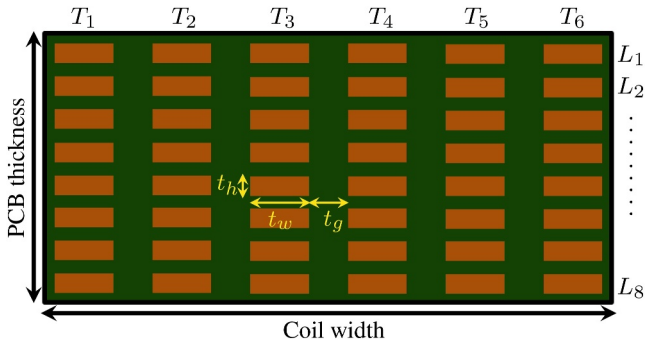

FIGURE 12 The cross section of a real PCB coil side with 6 turns and 8 layers, PCB manufacturers can produce up to 32-layer PCBs. Designers aim to maximise copper area to coil side area ratio, that is, higher slot fill factors to reduce Joule losses. PCB, printed circuit board.

layers per coil, and average length of the coil are denoted by N_t, N_L, and L_m, respectively. The slot fill factor is defined as follows:

$$SFF = \frac{N_t \cdot N_L \cdot A_t}{A_c}. \tag{13}$$

Substituting Equation (12) into Equation (11) we have the following:

$$P_{cu} = \frac{\rho \cdot L_m \cdot (N_L \cdot N_t \cdot I)^2}{A_c \cdot SFF}. \tag{14}$$

It is assumed that both the simplified and the real coil have the equivalent Ampere-turn, that is, $(N_L.N_t.I)$ to produce the same output torque. Therefore, with respect to Equation (14), the copper losses of the real coil, $P_{cu,R}$ is derived by scaling the copper losses of the simplified coil, $P_{cu,S}$, with the ratio of SFFs:

$$\frac{P_{cu,S}}{P_{cu,R}} = \frac{SFF_R}{SFF_S}. \tag{15}$$

The error of the scaled Joule losses with only one FEA solution relying on the equivalent 6-turn PCB coil is reported in Table 4. In comparison to the macro coil model, the copper loss estimation error was reduced by one-third. As Joule losses constitute the majority of losses in coreless machines the accuracy of the Joule loss estimation plays an important role in the machine performance analysis.

It is worth noting that, theoretically, 3D FEA models could be substituted by multi-stage 2D models as suggested in refs. [12, 14]. However, with the current state-of-the-art computational resources and software capabilities, the parametric 3D FE models utilising the proposed computationally efficient analysis method can be directly integrated into the machine design process within minutes. This approach significantly streamlines the process, eliminating the need to invest time in generating multi-slice 2D models and associated busy work. Moreover, the proposed method overcomes the typical simplifications inherent in 2D models, which may lack accuracy in the case of axial flux machines, while still maintaining the precision of 3D FEA models and completing computations within minutes.

4 | EXPERIMENTAL VALIDATION

The proposed approach is experimentally validated on a double-sided, two-phase coreless AFPM machine with a central 26-pole PCB stator. The two rotors are the same with 26 surface-mounted NdFeB magnets. This machine is designed to produce a rated torque of 19 Nm at 2,100 rpm with a fixed DC bus voltage of 300 V. The principle of operation and the specifications for this machine were described in detail by the authors in the previous papers [33, 34]. A test fixture has been designed and assembled to test the prototype machine at varying air-gap lengths, rotor numbers, phase numbers, and stator stacking schemes. Also, a5 hp servo motor is coupled with the coreless AFPM machine under study as a prime mover to measure back-EMF as shown in Figure 13.

4.1 | Single-phase Back-EMF

The measured single-phase back-EMF at 1000 rpm within one electrical cycle is illustrated in Figure 14. This figure also shows the back-EMF waveform, which was calculated by using Equation (6) and only two FE solutions from the simplified 3D FEA model of the machine. Comparing these waveforms shows that the proposed method can successfully estimate the back-EMF of the designed machine with minimum effort FE analysis.

4.2 | Single-phase electromagnetic torque

To investigate the accuracy of the proposed approach to predicting the output torque, the static torques at different rotor positions within half of an electric cycle are measured and compared with results of the proposed method in Figure 15. This figure shows good agreement between the experimental measurements and the calculated torque waveform based on Equation (7). The observed variation can be explained by a variety of factors, including the backlash of the locking mechanism, the PCB manufacturing tolerances, imperfect magnet placements, and magnet properties.

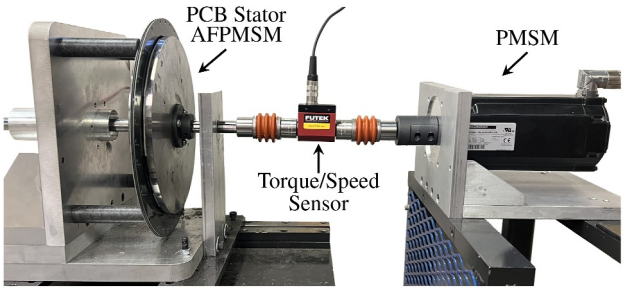

FIGURE 13 The test rig for the prototype 26-pole double-rotor single-stator coreless AFPM with printed circuit board stator connected to a PM synchronous machine as prime mover.

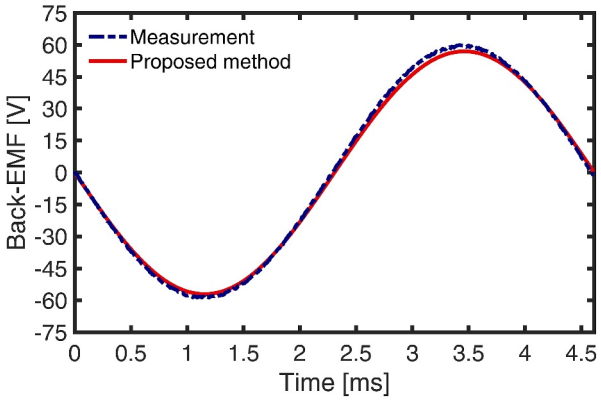

FIGURE 14 Single phase comparison of the experimental back-EMF waveforms and the estimated back-EMF relying on the simplified model and proposed approach with the minimum finite element analysis solutions at 1000 rpm.

5 | DISCUSSION

5.1 | Saturation effect and minimum number of FEA solutions

To ensure accurate results, the maximum order of harmonics determines the number of FEA solutions used in the suggested method. The use of a very low number of FEA solutions may be adequate if the airgap flux density is sinusoidal or quasi-sinusoidal due to a lack of saturation effects and low armature reaction, which is mostly the case for coreless AFPM machines.

In some designs, a very thin back iron needs to be considered due to mechanical considerations, and it may cause saturation. The effect of rotor back iron thickness on the performance of coreless machines was investigated in ref. [40]. In the presence of saturation, the accuracy of the results may be affected by an aliasing effect if the maximum harmonic order considered is lower than the order of harmonics that still have a meaningful contribution.

To avoid this, the harmonic analysis should be carried out, and more FEA solutions might be used, taking into consideration that each of them will only slightly increase computing work while adding more accuracy to the results. In this case, the introduced method can also be combined with the space-time transformation approach described in ref. [16]. Establishing a common and accurate foundation for comparison is challenging since a range of parameters, such as meshing, non-linear convergence, and so on, may exert a major influence.

5.2 | Stator design considerations: Torque ripple minimisation, equivalent conductor length, and design scaling

As mentioned in Section 2.3, considering an independent set of windings for each phase, in this case, one PCB stator per

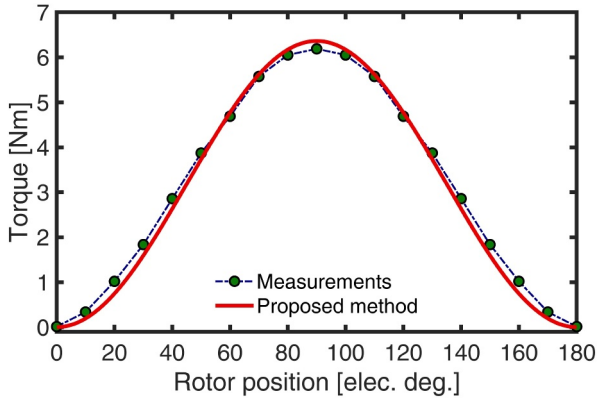

FIGURE 15 Measured and calculated static torque of the prototype printed circuit board stator coreless AFPM machine with a current density of 18 A/mm^2. The estimated torque waveform with the proposed approach is fairly comparable with measured static torques.

phase, results in torque ripple caused by the flux fringing effect and unequal distances of phase windings to the rotor magnets. To mitigate this torque ripple, one potential solution in this case is to design all three phases on a single PCB stator. However, this approach makes the implementation very challenging and complicated. Another approach could be to consider two identical sets of windings, that is, two PCB stators per phase, and distribute the phases as A-B-C-A-B-C in the axial direction.

In AFPM machines, the electromagnetic torque is generated through tangential forces, F_r, over a continuum of radial elements. The output torque can thus be calculated analytically from the Lorentz force law as the integral across stator conductor elements, dr, in the radial direction when they carry the coil current, i_c, and are exposed to airgap flux density, B_z, in the axial direction:

$$\mathrm{d}T = r\mathrm{d}F_r = (i_c \times B_z) r \mathrm{d}r. \tag{16}$$

For fast torque estimation, Equation (16) can be written as follows:

$$\widehat{T}_{ph} = N_c \cdot N_t \cdot \overline{B} \cdot \widehat{I}_c \cdot r_m \cdot L_m, \tag{17}$$

where $\overline{B}$ and $\widehat{I}_c$ are the average magnetic flux density over one coil side and the maximum input current in coils at 90 electrical degrees, where maximum torque occurs, respectively. The shaft distance to the middle of the coils is also depicted by r_m. The total number of coils and total the number of turns per coil are denoted by N_c and N_t, respectively. The torque producing active radial length of PCB conductors (area enclosed by red dashed line) and the average radial length for the coil, L_m are shown in Figure 11d.

By accurately estimating the average active radial length, the output torque produced at a specific outer diameter and flux density can be calculated and scaled for different dimensions effortlessly, without the need for time-consuming FE analysis.

To estimate average active radial length, (17) is solved for different values of L_m ranging from the length of the innermost turn to the outermost turn, and the results are compared with the FEA results of the initial design as shown in Figure 16. In this figure, lengths are normalised and the corresponding normalised active length, to zero error, L_{mN}, is used for calculating L_m for different designs. Considering the ratio of stator length to rotor length for the initial and new design, k_{r1} and k_{r2}, that determines how rotor magnets cover the stator conductors, the average active length for the new design, L_{m2}, can be calculated as follows:

$$L_{m2} = r_{i2} + \frac{k_{r2}}{k_{r1}}(r_{o2} - r_{i2}) L_{mN}, \tag{18}$$

where r_{i2} and r_{o2} are the inner and outer stator radius of the new design, respectively.

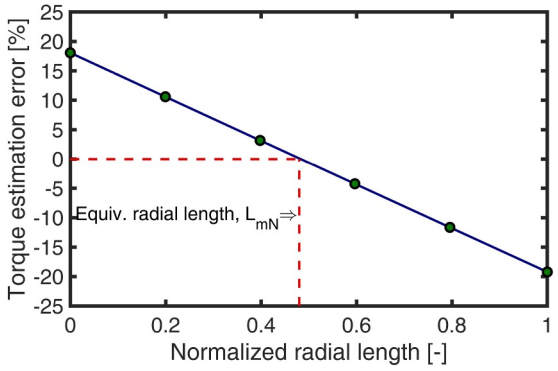

FIGURE 16 Analytical study to find the average active radial length of the coil conductors used for fast torque estimation and design scaling. Corresponding normalised radial length, L_{mN}, to zero torque estimation error is used for design scaling based on (18).

5.3 | Example optimisation study employing the proposed approach

The scripting features of commercially available electromagnetic FEA software can be used to practically implement the proposed approach. The block diagram of a design optimisation study for a coreless AFPM machine with concentric PCB coils based on conventional DE is demonstrated in Figure 17. Design optimisation was done by linking ANSYS Electronics Desktop and MATLAB through scripting to implement the proposed method.

In this optimisation study, more than 250 candidate designs were evaluated within lower than 24 h on the introduced workstation towards finding optimum designs with higher efficiency and lower magnet weight. Six independent variables, including those that determine the PCB coil geometry (shown in Figure 11d) were considered in this study. Without employing the proposed CE-FEA model and the estimation techniques, it is highly challenging to analyse this many accurate and complicated 3D FE models in a short amount of time. The model simplification process and the proposed estimation technique are not limited by the concentric coil shape and can be developed for various winding topologies effortlessly.

6 | CONCLUSION

This research proposed a computationally efficient simplified 3D FE model for coreless AFPM machines analysis. This model makes full use of the machine's geometric symmetry followed by a systematic strategy to figure out the minimum number of transient FE solutions that are required to accurately predict the machine performance indices like the output electromagnetic torque, copper losses, flux linkage, and back-EMF, which are critical to the design process. A simplified reduced-turn model for stator coils with planar conductors was also proposed to further reduce the computation time.

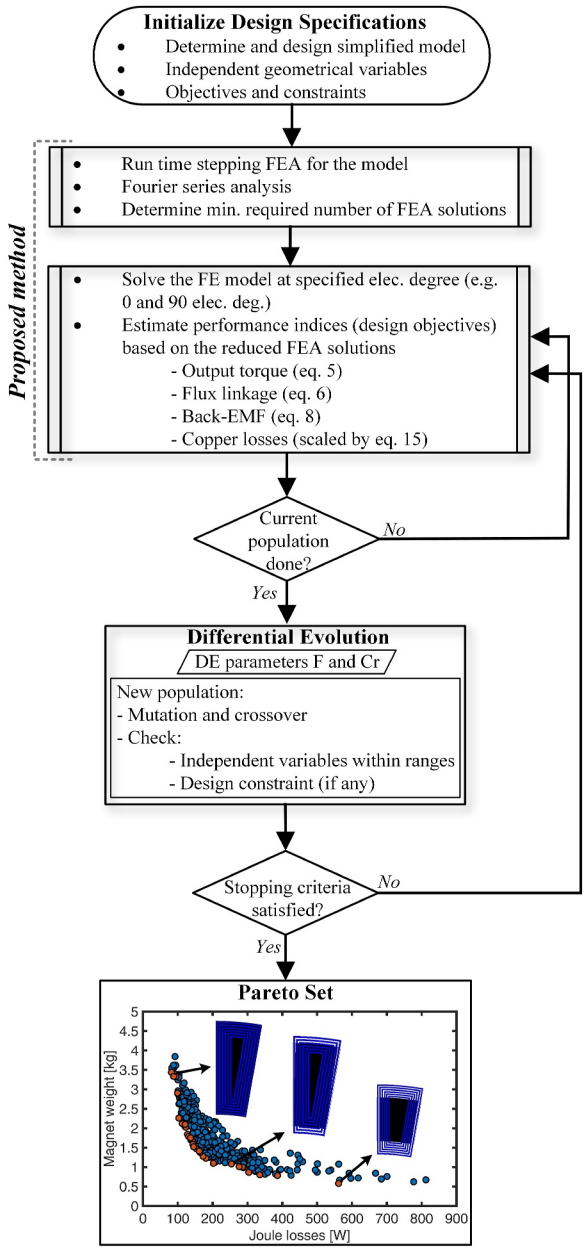

FIGURE 17 Block diagram for model-based design optimisation of a coreless AFPM with printed circuit board stator procedure employing the proposed ultrafast method.

Employing all the aforementioned techniques leads to a substantial reduction in the computational burden, providing an opportunity to incorporate accurate 3D FEA models into large-scale design optimisations. For example, the computational time of the 3D FEA model of a coreless AFPM machine with an 18-turn PCB coil and 36 time steps was reduced by two orders of magnitude, from 3.4 h to only 3.8 min, while maintaining the estimation error below 3% compared to the detailed real coil model.

The accuracy of the proposed computationally efficient model was verified by comparing the estimated and experimentally measured machine performance indices, that is, back-EMF and output torque, indicating very good agreement.

AUTHOR CONTRIBUTIONS

Yaser Chulaee: Conceptualization; data curation; formal analysis; investigation; methodology; validation; visualization; writing – original draft. **Dan M. Ionel:** Conceptualization; funding acquisition; methodology; project administration; resources; software; supervision; writing – review & editing.

ACKNOWLEDGEMENTS

The authors are most grateful to Professor J. F. Eastham of the University of Bath, England, for technical discussions, review, and feedback. This paper is based upon work supported by the National Science Foundation (NSF) under Award No. #1809876. Any opinions, findings, and conclusions or recommendations expressed in this material are those of the authors and do not necessarily reflect the views of the NSF. The support of ANSYS Inc., Regal Rexnord, and University of Kentucky the L. Stanley Pigman Chair in Power Endowment is also gratefully acknowledged.

CONFLICT OF INTEREST STATEMENT

We declare that we have no conflict of interest.

DATA AVAILABILITY STATEMENT

The data that support the findings of this study are available from the corresponding author upon reasonable request.

ORCID

Yaser Chulaee https://orcid.org/0000-0001-6189-3218
Dan M. Ionel https://orcid.org/0000-0002-7550-1972

REFERENCES

1. Rosu, M., et al.: Multiphysics simulation by design for electrical machines, power Electronics and drives. J. Wiley - IEEE Press (2017). https://doi.org/10.1002/9781119103462
2. Gardner, M.C., et al.: Optimization of coaxial magnetic gear design and magnet material grade at different temperatures and gear ratios. IEEE Trans. Energy Convers. 36(3), 2493–2501 (2021). https://doi.org/10.1109/tec.2021.3054806
3. Huang, C., et al.: Multi-objective optimization design of a stator coreless multidisc axial flux permanent magnet motor. Energies 15(13), 4810 (2022). https://doi.org/10.3390/en15134810
4. Taran, N., et al.: Systematically exploring the effects of pole count on the performance and cost limits of ultrahigh efficiency fractional hp axial flux PM machines. IEEE Trans. Ind. Appl. 56(1), 117–127 (2020). https://doi.org/10.1109/tia.2019.2943814
5. Mohammadi, A., et al.: Axial flux permanent magnet vernier machine with single-wound dual-stator and spoke permanent magnet rotor for electric vehicle in-wheel traction. In: 2023 IEEE Transportation Electrification Conference Expo (ITEC), pp. 1–5 (2023)
6. Subotic, I., et al.: Weight optimisation of coreless axial-flux permanent magnet machines. IET Electr. Power Appl. 13(5), 594–603 (2019). https://doi.org/10.1049/iet-epa.2018.5228
7. Taran, N., Ionel, D.M., Dorrell, D.G.: Two-level surrogate-assisted differential evolution multi-objective optimization of electric machines using 3-d fea. IEEE Trans. Magn. 54(11), 1–5 (2018). https://doi.org/10.1109/tmag.2018.2856858
8. Sato, H., Igarashi, H.: Fast multi-objective optimization of electromagnetic devices using adaptive neural network surrogate model. IEEE Trans. Magn. 58(5), 1–9 (2022). https://doi.org/10.1109/tmag.2022.3150271
9. Cao, Y., et al.: Analysis of analytical magnetic field and flux regulation characteristics of axial-flux permanent magnet memory machine. IEEE

Trans. Magn. 58(9), 1–9 (2022). https://doi.org/10.1109/tmag.2022.3194366
10. Xia, Z.P., Zhu, Z.Q., Howe, D.: Analytical magnetic field analysis of halbach magnetized permanent-magnet machines. IEEE Trans. Magn. 40(4), 1864–1872 (2004). https://doi.org/10.1109/tmag.2004.828933
11. Carpi, T., et al.: 3-d hybrid model of the axial-flux motor accounting magnet shape. IEEE Trans. Magn. 58(5), 1–4 (2022). https://doi.org/10.1109/tmag.2019.2950892
12. Gulec, M., Aydin, M.: Implementation of different 2d finite element modelling approaches in axial flux permanent magnet disc machines. IET Electr. Power Appl. 12(2), 195–202 (2018). https://doi.org/10.1049/iet-epa.2017.0434
13. Wang, X., et al.: Design and analysis of coreless axial flux permanent magnet machine with novel composite structure coils. Energies 15(14), 5162 (2022). https://doi.org/10.3390/en15145162
14. Kim, K.H., Woo, D.K.: Novel quasi-three-dimensional modeling of axial flux in-wheel motor with permanent magnet skew. IEEE Access 10, 98842–98854 (2022). https://doi.org/10.1109/access.2022.3206774
15. Ionel, D.M., Popescu, M.: Finite-element surrogate model for electric machines with revolving field—application to iPM motors. IEEE Trans. Ind. Appl. 46(6), 2424–2433 (2010). https://doi.org/10.1109/tia.2010.2073671
16. Ionel, D.M., Popescu, M.: Ultrafast finite-element analysis of brushless PM machines based on space–time transformations. IEEE Trans. Ind. Appl. 47(2), 744–753 (2011). https://doi.org/10.1109/tia.2010.2102733
17. Liu, Y., et al.: A simplified finite-element model of hybrid excitation synchronous machines with radial/axial flux paths via magnetic equivalent circuit. IEEE Trans. Magn. 53(11), 1–4 (2017). https://doi.org/10.1109/tmag.2017.2696568
18. Sergeant, P., et al.: A computationally efficient method to determine iron and magnet losses in vsi-pwm fed axial flux permanent magnet synchronous machines. IEEE Trans. Magn. 50(8), 1–10 (2014). https://doi.org/10.1109/tmag.2014.2308904
19. Wu, D., Pekarek, S.D., Fahimi, B.: A field reconstruction technique for efficient modeling of the fields and forces within induction machines. IEEE Trans. Energy Convers. 24(2), 366–374 (2009). https://doi.org/10.1109/tec.2008.2001439
20. Bianchi, N., Alberti, L.: Mmf harmonics effect on the embedded fe analytical computation of PM motors. IEEE Trans. Ind. Appl. 46(2), 812–820 (2010). https://doi.org/10.1109/tia.2010.2041098
21. Chen, X., et al.: A high-fidelity and computationally efficient model for interior permanent-magnet machines considering the magnetic saturation, spatial harmonics, and iron loss effect. IEEE Trans. Ind. Electron. 62(7), 4044–4055 (2015). https://doi.org/10.1109/tie.2014.2388200
22. Lin, S., et al.: Temperature dependent reduced order iPM motor model based on finite element analysis. In: 2015 IEEE International Electric Machines & Drives Conference (IEMDC), pp. 543–549 (2015)
23. Billah, M.M., Martin, F., Belahcen, A.: A computationally effective method for iron loss estimation in a synchronous machine from a static field solution. In: 2020 International Conference on Electrical Machines (ICEM), vol. 1, pp. 751–757 (2020). https://doi.org/10.1109/icem49940.2020.9271020
24. Candelo-Zuluaga, C., et al.: Computationally efficient analysis of spatial and temporal harmonics content of the magnetic flux distribution in a PMsm for efficiency maps computation. In: 2020 International Conference on Electrical Machines (ICEM), vol. 1, pp. 415–421 (2020). https://doi.org/10.1109/icem49940.2020.9270900
25. Sizov, G.Y., et al.: Automated multi-objective design optimization of PM ac machines using computationally efficient fea and differential evolution. IEEE Trans. Ind. Appl. 49(5), 2086–2096 (2013). https://doi.org/10.1109/tia.2013.2261791
26. Zarko, D., et al.: Reduction of computational efforts in finite element-based permanent magnet traction motor optimization. IEEE Trans. Ind. Electron. 65(2), 1799–1807 (2018). https://doi.org/10.1109/tie.2017.2736485
27. Wang, X., et al.: Modeling and optimization of brushless doubly-fed induction machines using computationally efficient finite-element analysis. IEEE Trans. Ind. Appl. 52(6), 4525–4534 (2016). https://doi.org/10.1109/tia.2016.2593715
28. Habib, A., et al.: A systematic review on current research and developments on coreless axial-flux permanent-magnet machines. IET Electr. Power Appl. 16(10), 1095–1116 (2022). https://doi.org/10.1049/elp2.12218
29. Zhang, Y., Wang, Y., Gao, S.: 3-d magnetic equivalent circuit model for a coreless axial flux permanent-magnet synchronous generator. IET Electr. Power Appl. 15(10), 1261–1273 (2021). https://doi.org/10.1049/elp2.12092
30. Rallabandi, V., et al.: Coreless multidisc axial flux PM machine with carbon nanotube windings. IEEE Trans. Magn. 53(6), 1–4 (2017). https://doi.org/10.1109/tmag.2017.2660526
31. Paul, S., et al.: A comparative analysis of wave winding topologies and performance characteristics in ultra-thin printed circuit board axial-flux permanent magnet machine. IET Electr. Power Appl. 13(5), 694–701 (2019). https://doi.org/10.1049/iet-epa.2018.5417
32. Salim, N., et al.: Multiphysics analysis of printed circuit board winding for high-speed afPM motor. IET Electr. Power Appl. 13(6), 805–811 (2019). https://doi.org/10.1049/iet-epa.2018.5752
33. Lawhorn, D., et al.: On the design of coreless permanent magnet machines for electric aircraft propulsion. In: 2021 IEEE Transportation Electrification Conference & Expo (ITEC), pp. 278–283 (2021)
34. Han, P., et al.: Design optimization and experimental study of coreless axial-flux PM machines with wave winding pcb stators. In: 2021 IEEE Energy Conversion Congress and Exposition (ECCE), pp. 4347–4352 (2021)
35. Marcolini, F., et al.: Design of a high speed printed circuit board coreless axial flux permanent magnet machine. In: 2021 IEEE Energy Conversion Congress and Exposition (ECCE), pp. 4353–4360 (2021)
36. Tokgöz, F., Çakal, G., Keysan, O.: Design and implementation of an optimized printed circuit board axial-flux permanent magnet machine. In: 2020 International Conference on Electrical Machines (ICEM), vol. 1, pp. 111–116 (2020). https://doi.org/10.1109/icem49940.2020.9271058
37. Tokgöz, F., Çakal, G., Keysan, O.: Comparison of pcb winding topologies for axial-flux permanent magnet synchronous machines. IET Electr. Power Appl. 14(13), 2577–2586 (2020). https://doi.org/10.1049/iet-epa.2020.0622
38. Wang, X., Li, C., Lou, F.: Geometry optimize of printed circuit board stator winding in coreless axial field permanent magnet motor. In: 2016 IEEE Vehicle Power and Propulsion Conference (VPPC), pp. 1–6 (2016)
39. Rallabandi, V., Taran, N., Ionel, D.M.: Multilayer concentrated windings for axial flux PM machines. IEEE Trans. Magn. 53(6), 1–4 (2017). https://doi.org/10.1109/tmag.2017.2661312
40. Chulaee, Y., et al.: Torque and power capabilities of coreless axial flux machines with surface PMs and halbach array rotors. In: 2023 IEEE International Electric Machines Drives Conference (IEMDC), pp. 1–6 (2023)
41. Ansys Electronics Desktop, Maxwell, Version 231, 2023, ANSYS Inc
42. Chulaee, Y., et al.: Design optimization considering a detailed pcb stator layout for coreless afpm machines with minimal eddy and circulating current losses. In: 2023 IEEE Energy Conversion Congress and Exposition (ECCE), pp. 3753–3758 (2023)
43. Chulaee, Y., et al.: Circulating and eddy current losses in coreless axial flux PM machine stators with pcb windings. IEEE Trans. Ind. Appl. 59(4), 1–11 (2023). https://doi.org/10.1109/tia.2023.3267026
44. Sullivan, C.R.: Optimal choice for number of strands in a litz-wire transformer winding. IEEE Trans. Power Electron. 14(2), 283–291 (1999). https://doi.org/10.1109/63.750181
45. Fatemi, A., et al.: Computationally efficient strand eddy current loss calculation in electric machines. IEEE Trans. Ind. Appl. 55(4), 3479–3489 (2019). https://doi.org/10.1109/tia.2019.2903406

46. Popescu, M., Dorrell, D.G.: Skin effect and proximity losses in high speed brushless permanent magnet motors. In: 2013 IEEE Energy Conversion Congress and Exposition, pp. 3520–3527 (2013)
47. Chulaee, Y., et al.: Circulating and eddy current losses in coreless axial flux PM machine stators with PCB windings. IEEE Trans. Ind. Appl. 59(4), 4010–4020 (2023). https://doi.org/10.1109/tia.2023.3267026

How to cite this article: Chulaee, Y., Ionel, D.M.: Ultra-fast finite element analysis of coreless axial flux permanent magnet synchronous machines. IET Electr. Power Appl. 18(8), 883–896 (2024). https://doi.org/10.1049/elp2.12439